JOURNAL OF SOLID STATE CHEMISTRY 58, 56–70 (1985)

Structural Evolution of Manganosite: Comparison of Properties of Nonstoichiometric Manganese and Iron Monoxides

JEAN-RAYMOND GAVARRI,* JACEK ARABSKI,† STANISŁAWA JASIENSKA,† JAN JANOWSKI,† AND CLAUDE CAREL‡

**Laboratoire de Chimie Physique du Solide, U.A. au CNRS No. 453, École Centrale des Arts et Manufactures, 92290 Châtenay-Malabry and Université Paris 13, Avenue J.-B. Clément 93430 Villetaneuse, France; †Akademia, Górniczo-Hutnicza, Instytut Metalurgii, Aleja Mickiewicza 30–059 Krakow, Poland; and ‡Laboratoire de Cristallochimie, L.A. au CNRS No. 254, Avenue du Général Leclerc, 35042 Rennes Cédex, France*

Received July 11, 1984; in revised form October 17, 1984

Accurate measurements of the lattice parameters of polycrystalline manganosite $Mn_{1-z}O$ lead to the conclusion that the magnetic lattices of the stoichiometric MnO and Mn_3O_4, which appear during the cooling process, do not interact. The X-ray energetic shifts and the morphology of the manganosite are described for multilayer samples obtained by oxidation of the metal. The reactivity of the two isomorphic monoxides, $Mn_{1-z}O$ or manganosite and $Fe_{1-z}O$ or wüstite, is interpreted in terms of the elastic constant C_{44}. The clustering of the point defects, the deformation energy, and the comparative plasticity or brittleness are discussed in terms of this constant for both monoxides at high temperature and after quenching.

Introduction

For several years, structural techniques have been developed to study the evolution of physical properties of polycrystalline materials. In particular, low temperature diffraction analysis between 5 and 300 K has related the thermal expansion of the lattice and bonds with macroscopic and local elastic properties. The point defects due to nonstoichiometry produced during synthesis can induce steric anharmonic vibrational effects and changes in magnetic properties, e.g., magnetostriction. X-ray diffraction allows the study of these anisotropic effects and symmetry changes due to perturbations of the host lattice.

In this paper, manganosite is compared with iron monoxide, or wüstite, because of their isomorphic NaCl-type structure above the Néel temperature (*1–5*). From the thermodynamic point of view, the molar formation enthalpy, entropy, and free energy show a large difference for both monoxides with nearly the same departure from the stoichiometry. Wüstite with its limiting composition is in equilibrium with γ-Fe at 1400 K following the chemical equation

$$0.951\gamma\text{-Fe} + \tfrac{1}{2}O_2 \rightleftarrows Fe_{1-0.049}O.$$

From the numerical relation (4) given in Ref. (*6*), the values of the thermodynamic properties are deduced at this temperature:

0022-4596/85 $3.00

$$\Delta H^{\circ}_{f\,1400}(Fe_{0.951}O) = -262.9 \text{ kJ/mole},$$

$$\Delta S^{\circ}_{f\,1400}(Fe_{0.951}O) = -64.5 \text{ J/(K} \cdot \text{mole)},$$

$$\Delta G^{\circ}_{f\,1400}(Fe_{0.951}O) = -172.6 \text{ kJ/mole}.$$

In the course of the calculation of a new phase diagram of manganosite (7–9), according to the chemical equation

$$6.881Mn_{1-0.032}O + O_2 \rightleftarrows 2.220Mn_3O_4,$$

at 1400 K, the following values have been obtained:

$$\Delta H^{\circ}_{f\,1400}(Mn_{0.968}O) = -381.2 \text{ kJ/mole},$$

$$\Delta S^{\circ}_{f\,1400}(Mn_{0.968}O) = -80.0 \text{ J/(K} \cdot \text{mole)},$$

$$\Delta G^{\circ}_{f\,1400}(Mn_{0.968}O) = -269.3 \text{ kJ/mole}.$$

These significantly different values should be taken into consideration for physical properties related to the energy.

1. Manganosite—Experiments and Interpretation of Results

1.1. Phase Diagram

When comparing the thermodynamic conditions of existence of the wüstite FeO_x and the manganosite MnO_x, several analogies are found. Such a comparison was already partly made in Ref. (*8*). The equilibrium phase field of manganosite has been defined by means of the projection of the state diagram on the plan (θ°C, x) (Fig. 1). Different varieties or behaviors are taken into account (*5–9*). The set of the isobaric curves for the equilibrium oxygen pressure above the solid phase has been calculated (*9*) and is drawn in Fig. 1. It has been partly confirmed using electron microprobe analysis.[1]

Measurements of the $K\alpha$ emission band intensities have been performed in order to evaluate the chemical composition which has been determined on 2 quenched multilayer oxidized samples (see Section 1.4). So, the limiting compositions (x_0, x_1) on the external boundaries of the manganosite phase diagram have been obtained experimentally: x_0 and x_1 concern the Mn/MnO_{x_0} and MnO_{x_1}/Mn_3O_4 boundaries, respectively. They are in agreement with those derived by thermodynamic calculations (*8*, *9*) (Table I), particularly on the $Mn/Mn_{1-z_0}O$ boundary (*Cf.* ■ in Fig. 1).

[1] Electronic microprobe CAMEBAX manufactured by the society CAMECA; experiments performed at A.G.H. (Krakow).

1.2. Samples

The preparation of samples of manganosite is rather difficult, more difficult than the preparation of similar samples of wüstite because of the higher temperature, slower rate of diffusivity of the manganese ions, and lower equilibrium partial pressures of oxygen. Many samples were prepared under CO_2/CO gas mixtures at temperatures from 1200 to 1450°C in a vertical furnace, then quenched by either being dropped into water or cooled on the wall of a water jacket under the equilibrium atmosphere. Some of them were studied (*10*) (Table II). They are located in the state diagram in Fig. 1 (sign ●).

1.3. X-ray Diffraction Studies

The X-ray analysis of quenched polycrystalline samples was performed between 4 and 300 K by cooling and heating in a cryostat and using a very accurate diffractometer. The confidence limit in the measurement of the angles is $\Delta\theta_{Bragg} = \pm 2 \times 10^{-3}\theta$ (*11*). The parameters of the trigonal

TABLE I

Quenching temperature	Measured composition[a]	Calculated composition
1050	$x_0 = 0.98$ or $z_0 = -0.02$	$x_0 = 0.9824$ or $z_0 = -0.0179$
	$x_1 = 1.02$ or $z_1 = 0.02$	$x_1 = 1.0208$ or $z_1 = 0.0204$
1150	$x_0 = 0.98$ or $z_0 = -0.02$	$x_0 = 0.9800$ or $z_0 = -0.0204$
	$x_1 = 1.035$ or $z_1 = 0.03$	$x_1 = 1.0365$ or $z_1 = 0.0352$

[a] $\Delta z \sim (\pm 0.01)$.

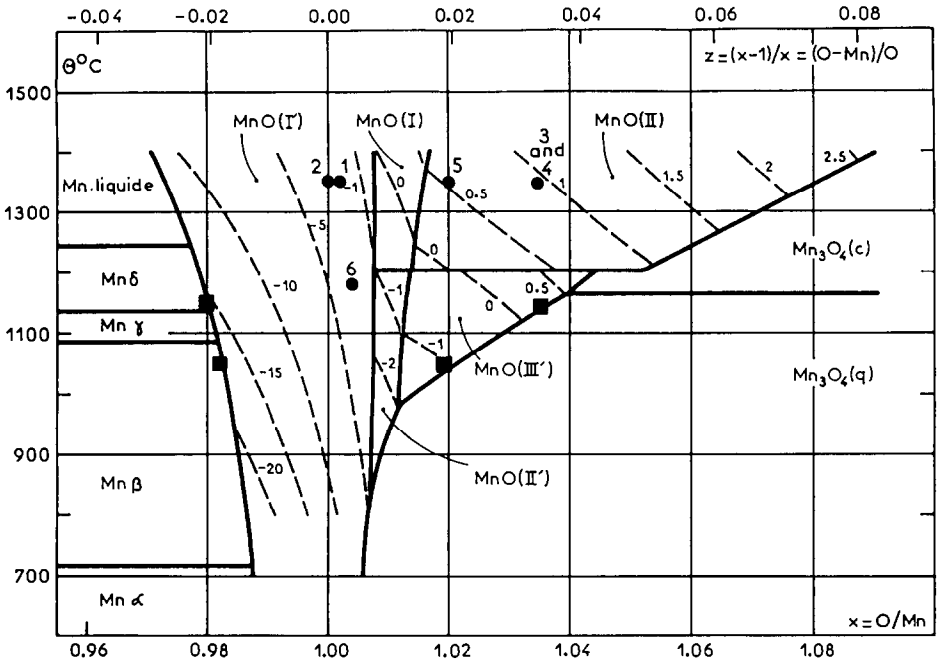

FIG. 1. Location (●) in the state diagram of the manganosite samples before quenching. The dashed curves correspond to constant P_{O_2} expressed in Pascal. The number near each curve with its sign is the power of ten of the oxygen pressure. The four ■ indicate the composition measured by electron microprobe in an oxidized multilayer sample at the interfaces Mn/MnO and $Mn_{1-z}O/Mn_3O_4$ at 1050 and 1150°C.

cell (a_R and $\alpha_R > 90°$) have been determined from the Bragg peaks (111), (200), and (220). A part of the present results has been published (*10*).

Hausmannite Mn_3O_4 was always detected after quenching when the equilibrium nonstoichiometric composition is such that $z > 0.002$ (*10, 12*). The amount of Mn_3O_4 is consistent with the chemical composition before quenching (*8, 9*) and shows that the monoxide is nearly stoichiometric. The variation of a_R as a function of z observed by Touzelin *et al.* (*13*) has not been observed in this study because of the dis-

TABLE II

Sample No.	$p(CO)/p(CO_2)$	T (K)	x = O/Mn under equilibrium	Quenching rate	Color	Mn_3O_4[a] (%)	$a(\sigma)$ (Å)
1	10/90	1623	1.002	Fast	Brown-green	No	4.4442(2.6)
2	18/82	1623	1.000	Slow	Green	No	4.4455(2.4)
3	0.3/99.7	1623	1.035	Fast	Brown	3	4.4446(2.7)
4	0.3/99.7	1623	1.035	Slow	Brown-green	3	4.4442(2.4)
5	0.5/99.5	1623	1.020	Slow	Dark green	1.3	4.4455(2.8)
6	2/98	1453	1.004	Slow	Brown-green	No	4.4446(2.8)

[a] Detected and evaluated from X-ray diffraction patterns (Mo$K\alpha$).

TABLE III

T (K)	Sample 2: $x = 1.00$[a] a_R (Å)	α_R (°)	V_R (Å^3)	Sample 3: $x = 1.04$[a] a_R (Å)	α_R (°)	V_R (Å^3)
5	4.4327	90.605	87.09	4.4317	90.598	87.04
35	4.4326	90.595	87.08	4.4317	90.587	87.03
50	—	—	—	4.4312	90.578	87.00
77	4.4334	90.509	87.15	4.4336	90.497	87.14
90	4.4339	90.449	87.16	4.4329	90.438	87.11
100	4.4335	90.367	87.14	4.4337	90.392	87.15
110	4.4339	90.284	87.17	4.4346	90.368	87.21
115	4.4344	90.234	87.20	4.4358	90.240	87.28
120	4.4356	89.998	87.27	4.4364	90.000	87.32
125	4.4366	90.001	87.33	4.4364	90.003	87.32
200	4.4394	(90.000)	87.49	4.4393	(90.000)	87.48
300	4.4454	(90.000)	87.84	4.4445	(90.000)	87.80

[a] Taking into account the experimental errors, the scattering of the results for a given temperature is not significant.

proportionation. The mean value of $\bar{a}$ is 4.4448(6) Å. The quasi-invariance of $\bar{a}$ in spite of the Mn_3O_4 precipitates has been discussed previously (*10*).

The magnetic transition. Table III gives the measured rhombohedral parameters a_R and α_R and the volume V_R of the corresponding cell as a function of the temperature for two samples (Nos. 2 and 3 in Table II). Figures 2a and b show the variations of a_R and α_R. These variations are quite similar for initially stoichiometric and nonstoichiometric samples.

The Néel temperature T_N is observed at 120 ± 2 K (*12* to *15*) in both cases. Figure 3 represents the separation $\Delta\theta$ of the (220) and ($2\bar{2}0$) Bragg peaks below T_N in the rhombohedral coordinates (*14–16*).

X-ray measurements in the neighborhood of T_N have been carried out. Pretransitional effects can be observed in Fig. 3. According to previous results on pressed monocrystals (*17*), the first-order character of the magnetic transition is partly removed by size effects and phase–antiphase domains.

Bloch *et al.* (*17*) gave the main significant equations characterizing the exchange striction.

Let $\alpha \sim \alpha_R - 90°$ be the distortion angle, J_1 the exchange integral between the first nearest neighbors, J_2 the exchange integral between the second nearest neighbors. Magnetostrictive effects may be characterized by

$$j_1 = (dJ_1/J_1)(dr_1/r_1)$$

$$j_2 = (dJ_2/J_2)(dr_2/r_2).$$

The magnetic energy involved in the distortion of the cell is given by

$$\Delta E_m = -\frac{6NS^2}{V}\left(j_1 J_1 \alpha - j_2 J_2 \frac{\Delta a}{a}\right) \quad (1)$$

where N is the Avogadro number, V the molar volume.

The elastic energy is given by

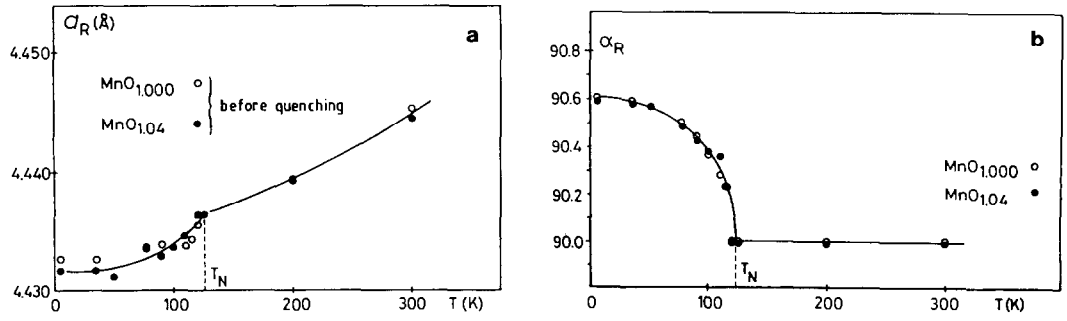

FIG. 2. (a) Linear parameter of the cubic or trigonal cell ($T > T_N$ or $T < T_N$) vs temperature for samples 2 and 3 in Table II quenched from 1300°C. (b) Angle of the cubic or trigonal cell ($T > T_N$ or $T < T_N$) vs temperature for samples 2 and 3.

$$E_{el} = \tfrac{3}{2}(C_{11} + 2C_{12})\left(\frac{\Delta a}{a}\right)^2 + \tfrac{3}{2}C_{44}\alpha^2. \quad (2)$$

The minimum of the total energy (E_{el} + ΔE_n) is obtained for

$$\frac{\Delta a}{a} = -\frac{2NS^2}{V} \cdot \frac{j_2 \cdot J_2}{C_{11} + 2C_{12}} \quad (3)$$

and

$$\alpha = \frac{2NS^2}{V} \cdot \frac{j_1 J_1}{C_{44}} \quad (4)$$

C_{11}, C_{12}, and C_{44} are the terms of the cubic elastic tensor.

The present results are congruent with some previous results (*17*) in spite of the strong temperature dependence of the C_{44} constant close to T_N (*18*). In addition because T_N is constant in our experiments (Fig. 3), the molecular field approximation suggests the invariance of J_2: $\frac{3}{2}k \cdot T_N = -6S \cdot (S + 1) \cdot J_2$. Because the terms T_N, $\Delta V/V$, and α_R do not vary with the primary composition before quenching, the coefficients j_i, the exchange integrals J_i, and the elastic constants must remain independent of the precipitate Mn_3O_4. So the two lattices of the manganosite and hausmannite are not connected.

One should notice that the presence of

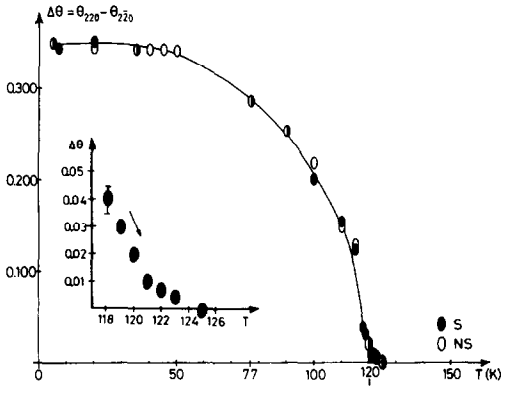

FIG. 3. Angular distortion below and above T_N (in degrees); close to T_N ($T > T_N$) pretransitional effects can be observed: they may be related to the strong C_{44} decrease observed by (*18*).

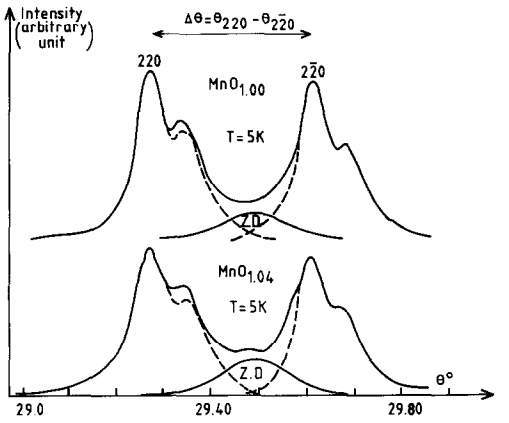

FIG. 4. Diffuse peak: the wall effect between phase–antiphase domains.

vacancies and Mn^{3+} ions diluted in the MnO host lattice should involve a simultaneous change of the mean values of $\bar{S}$, j, J (*14*) and probably of the quantities $(C_{11} + C_{12})^{-1}$ and C_{44}^{-1} [2]. As a result $\Delta a/a$ and α must vary in a significant fashion at a fixed temperature ($T < T_N$). That was not observed in our X-ray experiments (Figs. 2a and b) as indicated previously.

Profile analysis and nonstoichiometry. A broad residual peak related to the initial cubic structure ($T > T_N$) has been revealed by profile analysis of the two Bragg peaks (220) and (2$\bar{2}$0) of the rhombohedral antiferromagnetic phase. Its intensity increases with increasing initial nonstoichiometry. It is the greatest for the sample $MnO_{1.04}$. The presence of precipitate Mn_3O_4 might increase wall effects between ordered domains. It is well known that the antiferromagnetic spin ordering induces domains separated by walls in the cubic initial lattice. In quenched $MnO_{1.04}$ the full surface of the residual (220) cubic peak is practically twice as large as that in the stoichiometric sample (Fig. 4).

Grüneisen parameter. Table IV indicates

[2] The Mn^{3+}–O bonds are shorter and stronger than the Mn^{2+}–O bonds.

TABLE IV

T (K)	α_V (K^{-1})[a]	C_V (J/K · mole)	γ[b]
50	9.4	11.3	1.72
80	14.1	22.3	1.31
100	37.5	33.2	2.35
110	66	38.8	3.54
115	89	43.4	4.27
117.8	109	50.4	4.50
119	130	58.7	5.12
	Transition at T_N		
130	11.4	33.4	0.71
200	25.8	37.7	1.43
226	43.3	39.3	2.30
300	43.9	42.9	2.15

[a] From Table III.

[b] γ is calculated in assuming χ invariant. This approximation is not valid in the neighborhood of T_N, because of pretransitional effects.

the temperature dependence of the Grüneisen parameter

$$\gamma = \frac{\alpha_V \cdot V}{C_V \chi} = -\frac{V}{\theta_D} \cdot \frac{d\theta_D}{dV} \qquad (5)$$

where θ_D is the Debye temperature, α_V the volumic thermal expansion coefficient, and the compressibility χ is quasi-invariant. For the manganosite $\chi = 3(C_{11} + 2C_{12})^{-1} = 0.64 \times 10^{-11}$ Pa^{-1}. The specific heat data [C_V(MnO)] are evaluated from the results (*19, 20*) in the same way as in (*21*). The Grüneisen parameter characterizes the anharmonic behavior of a material as a function of the temperature. In case of the manganosite, the strong variation of γ obtained just below T_N corresponds to the $\alpha_V(T)$ variation.

1.4. Energetic Shifts

The $L\alpha_{1-2}$ X-ray emission band has been used to connect the energetic shift expressed by $\Delta\lambda_{L\alpha} = \lambda_{L\alpha}(\text{Mn}) - \lambda_{L\alpha}(\text{MnO}_x)$ with the ratio x = O/Mn measured separately by microprobe analysis. The shift $\Delta\lambda_{L\alpha}$ is found to be roughly proportional to z, the departure from stoichiometry (Fig. 5). This might indicate that small Mn_3O_4 islands modify the Mn^{2+} electronic levels ($3d$, $2p$) of the host MnO (*22*). So in multilayer samples both phases MnO and Mn_3O_4 would seem to interact, which is not the case with the polycrystalline samples.

After quenching from 1050°C, an empirical relation

$$\Delta\lambda_{L\alpha} = -0.055 + 0.058(1 + z) \qquad (6)$$

may be calculated for the variation of the shift $\Delta\lambda_{L\alpha}$ (Å) as a function of z. For z = 0.25, *i.e.*, for Mn_3O_4, the extrapolated value is $\Delta\lambda_{L\alpha} = 17 \times 10^{-3}$ Å. In the same experimental conditions, the value $\Delta\lambda_{L\alpha} = (26 \pm 1) \times 10^{-3}$ Å has been found for pure Mn_3O_4.

For an oxidation layer obtained at 1150°C, the relation

$$\Delta\lambda_{L\alpha} = -0.049 + 0.054(1 + z) \qquad (7)$$

appears to be significantly different from relation (6). That seems to show a large influence of the quenching temperature and process. The texture and the residual stresses might influence largely the amplitude of the shift. So these equations shall be considered only as a trend.

New analyses are planned to study the

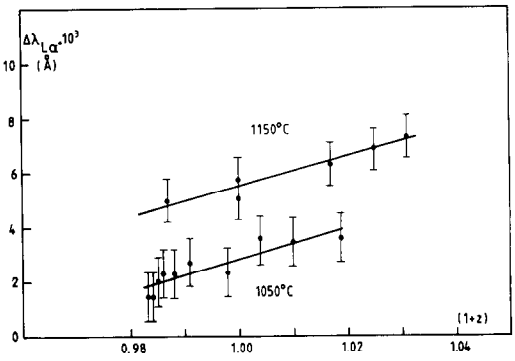

FIG. 5. Energetic shift spectroscopy throughout the manganosite layer: the shift is expressed by the variation in wavelength vs x = O/Mn at 1050 and 1150°C. $\Delta\lambda_{L\alpha} = \lambda_{L\alpha}(\text{Mn}) - \lambda_{L\alpha}(\text{MnO}_x)$.

TABLE V

	Self-diffusion coefficient[a]		Activation energy of the self-diffusion, E_A (kJ/mole)	Elastic constant[b]		
	$10^4 \cdot D_0$(m²/sec)	$10^4 \cdot D$(m²/sec) at 1300 K		C_{11}	C_{12}	C_{44}
				(10^{+11} Pa)		
$Fe_{1-z}O$	8.6×10^{-3}	9.8×10^{-8}	123	2.4	1.3	0.45
MnO	2.9×10^{-2}	5.0×10^{-11}	218	2.3	1.2	0.80

[a] $D = D_0 \exp(-E_A/RT)$ (*4, 23–26*).
[b] Components of the elastic tensor (*27–29*).

size of Mn_3O_4 islands or wüstite-like clusters in quenched manganosite.

2. Connection of the Elastic Constant C_{44} with Physical Properties

Taking into account various experimental facts, correlations may be established between the elastic properties (mainly the elastic constant C_{44}) and nonstoichiometry, clustering of point defects, self-diffusion, brittleness, and morphology.

Table V shows that the elastic constants C_{11} and C_{12} have nearly the same value for both monoxides, $Fe_{1-z}O$ and MnO, while C_{44} is twofold in MnO. In addition the activation energy of the self-diffusion is twice as large for manganosite as for wüstite.

2.1. Compressibility and Nonstoichiometry

The authors (*28, 29*) have observed in wüstite that the elastic constants C_{11} and C_{12} or the bulk modulus are not affected by nonstoichiometry. A likely interpretation of this feature is given below.

If the mean elastic potential is expressed in terms of a linear combination of microscopic potentials in the iron monoxide with the formula $Fe_{1-z}O = (Fe^{2+})^{octa}_{1-3z}(Fe^{3+})^{octa}_{2z-t}(Fe^{3+})^{tetra}_{t}(\square)_{z+t}O^{2-}$, one obtains

$$\langle E_{el} \rangle \sim E_1(FeO) - z(3E_1(FeO) - 2E_2) + t(E_3 - E_2) \quad (8)$$

where E_1, E_2, E_3 are respectively associated with the ions $(Fe^{2+})^{octa}$, $(Fe^{3+})^{octa}$, and $(Fe^{3+})^{tetra}$.

In first approximation, one generally makes the assumption that E_i ($i = 1$, 2, or 3) is principally related to the coulombic function qq'/r where q and q' are the effective charges of two next nearest ions, and r the interatomic distance ($q(Fe^{2+}) = 2$, $q'(Fe^{3+}) = 3$).[3] The numerical calculation leads to $E_2 \sim \frac{3}{2}E_1$, $E_3 \sim E_2$, with the experimental value $(z + t)/t \sim 2.4 \pm 0.4$ (*21, 30*). It follows that $E_{el} \sim E_1$, i.e., the elastic potential is quasi-invariant as z varies. As a consequence, the elastic constants C_{11} and C_{12} are invariant and so is the compressibility.

This simple interpretation cannot be applied to the angular interactions (O–*M*–O) and to C_{44} which might be strongly influenced by point defects.

After quenching, manganosite has a different defect structure than wüstite; there is a strong disproportionation (MnO/Mn_3O_4); so, the elastic constants cannot be affected in a significant way by the initial chemical composition ($Mn_{1-z}O$) because of the quasi-independence of the two lattices. The result is the same as in wüstite but the cause is different.

[3] Generally, the numerical contributions of repulsive interactions are negligible for the equilibrium positions: in addition they are assumed to be identical in each E_i expression.

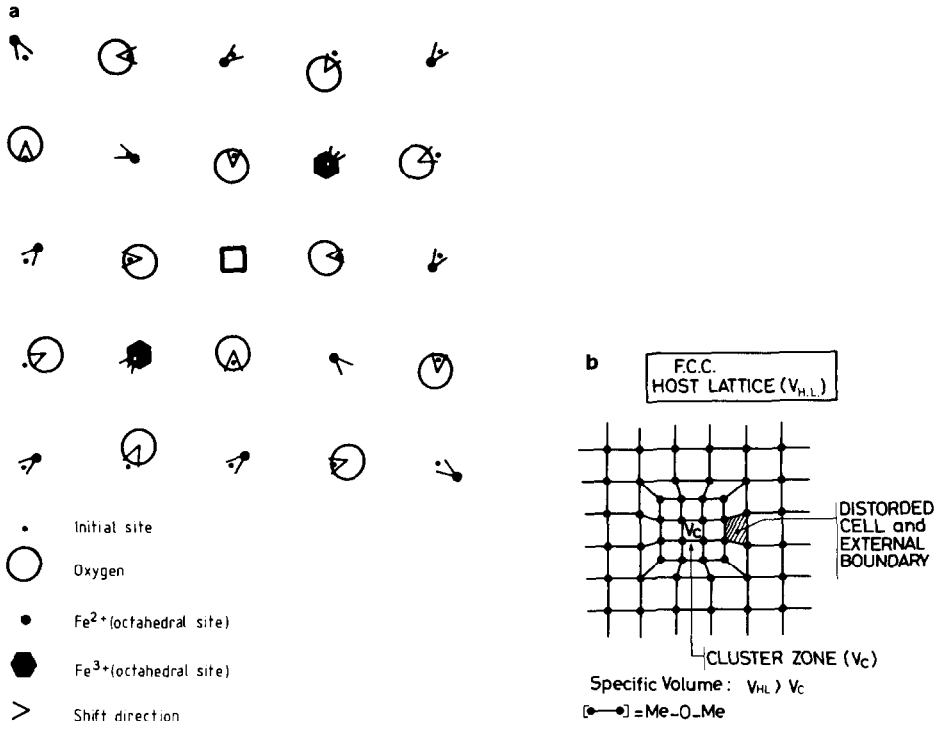

FIG. 6. (a) Static distortions due to a simple cluster $[Fe^{3+}]^{octa}$–□–$[Fe^{3+}]^{octa}$. (b) Schematic representation of a cluster zone with the specific volume V_C weaker than that of the cubic host lattice. The angular distortions are located in the boundary.

2.2. Elastic Distortion Energy Due to Point-Defect Clusters and Quenching

2.2.1. High temperature clustering. It has been suggested (*21*) that a simple point-defect cluster induces static shifts of the atoms (Fig. 6a) in wüstite. This may be extended to manganosite. It causes some distortions of the O–*M*–O angles, the *M*–O distances remaining nearly constant. The elastic deformation energy can be connected to the C_{44} constant of the elastic tensor because of the mean cubic symmetry. If α is the distortion angle, the elastic energy E_{el} is roughly proportional to $C_{44} \cdot \alpha^2$ (see (2), $\alpha_R = 90 + \alpha$).

Figure 6b represents a schematic view of a clustering zone (vacancies + insterstitial + M^{3+} surrounding cloud) in the fcc host lattice. The external boundary of the cluster is distorted in such a way that a failure of the cubic local symmetry arises: the O–*M*–O angles are distorted at least in this intermediate zone, the extension of which is not known. The whole elastic energy induced by the deformation of this zone is proportional to $(\tilde{C}_{11} + \tilde{C}_{12})(\Delta\tilde{a}/a)^2 + \tilde{C}_{44}\tilde{\alpha}^2$ (see Appendix 1). If "hard-sphere" atomic packing is postulated, the distortion component $\Delta a/a$ is negligible and the angular distortion is predominant. Generally this latter term is strong. The specific volumes of both host lattice and clustering are very different (Fig. 6b).

Taking into account the C_{44} values given in Table V, the elastic energy due to the angular distortion is larger in MnO than in wüstite for the same external surface of a cluster. It is obviously an increasing function of the total surface of the distorted

zones. It is minimized by the condensation of the clusters in zones as large as possible therefore as scarce as possible. So the likely clusters could be a priori larger in manganosite than in wüstite at high temperature.[4]

2.2.2. Quenching process. A crystal isolated during quenching is represented diagrammatically in Fig. 7a. Between the cold surface and the hot internal zone, the thermal stress gradient involves a continuous distortion with a total external angle ϕ which is the sum of the cell distortions $\delta\phi$ (Fig. 7a).

For large crystals a large stress gradient is involved because of the large value of ϕ. The migration of metal ions and vacancies occurs in two opposite directions where the specific volumes are larger and smaller, respectively (ascending diffusion).

The jumps of M^{2+} and M^{3+} cations can occur according to two principal paths: the well-known octa–octa path and the octa–tetra–octa path (*4, 31–34*). The octa–tetra jumps, even if less probable when considering self-diffusion processes, play a main role during the formation of the spinel structure. At room temperature, Fe^{3+} ions are stabilized in the tetrahedral sites of Fe_3O_4, but Mn^{2+} ions are located in tetrahedral sites of Mn_3O_4. So during quenching, some of the Mn^{2+} ions must jump from octa- to tetra positions, creating Mn_3O_4 islands.

Let us recall that these jumps are easier when vacancies are present in large concentrations. The existence of the well-known (m/n) clusters (m vacancies, n interstitials) clearly indicates that octa–tetra jumps are most likely in zones where vacancies are concentrated. Therefore,

[4] The equilibrium phase diagram of $Mn_{1-z}O$ is not as wide as that of wüstite. This difference could be connected to the existence of larger clusters in $Mn_{1-z}O$, which should precipitate more easily in giving the spinel oxide. Mn_3O_4 is a normal spinel contrary to Fe_3O_4.

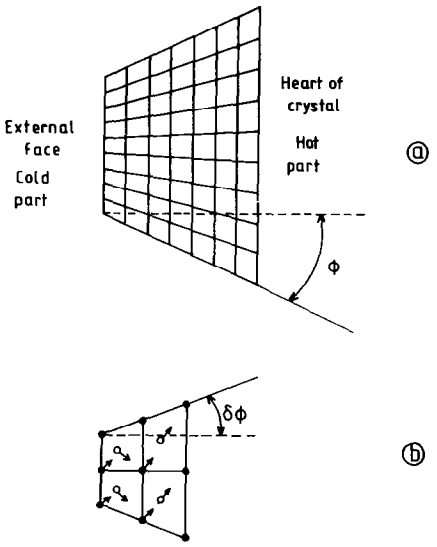

FIG. 7. Angular distortion of a crystal due to the thermal and stress gradients during quenching. In (a), ϕ is the whole angle as a result of the cooperative unit cell distortions $\delta\phi$. (b) (o→) = (octa–tetra–octa): the so-called ascending mechanism of diffusion [see Ref. (*4*, p. 183)].

around an Mn_3O_4 nucleus or cluster, these jumps can be collective and give rise to an Mn_3O_4 crystallite during quenching (Fig. 7b).

In addition, the formation of superclusters or precipitates during the quenching process minimizes the angular distortion, hence the stress gradient from the center to the surface of the crystals. This phenomenon is stronger in manganosite than in wüstite. These different features might explain why Mn_3O_4 is systematically present in quenched MnO while Fe_3O_4 is missing in $Fe_{1-z}O$ at least for $z < 0.10$.

2.3. Self-Diffusion of Cations

The jump of an atom from an octahedral site to a next nearest tetrahedral or octahedral site is the easiest when the oxygen atoms vibrate together with sufficiently large amplitudes to allow cation motions (*31*). This jump depends on a potential barrier (Fig. 8) which may be related in first ap-

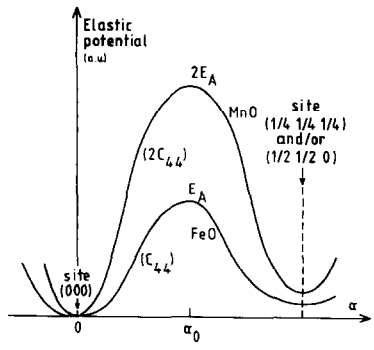

FIG. 8. General shape of the elastic potential barriers; a.u. = arbitrary unit; component function of α (angular distortion of bonds).

proximation to the activation energy E_A of the self-diffusion.

In the fcc structure, the two principal kinds of jump imply two energy barriers, E_A^1 (octa–octa) and E_A^2 (octa–tetra). Due to the existence of Fe^{3+} in tetrahedral sites in wüstite, it is not possible to rule out a significant contribution of octa–tetra jumps to the self-diffusion. In addition, the disproportionation process cannot be understood without the existence of collective octa–tetra motions initiating the spinel precipitation.

Appendix 2 gives a simple calculation relating the C_{44} constant to the activation energy E_A^1 for common case of octa–octa jumps. This model could be applied to octa–tetra jumps without important differences in the results. The experimental ratio C_{44}^{Mn}/C_{44}^{Fe} is equal to 1.778. The experimental ratio $E_A{}^{Mn}/E_A{}^{Fe}$ is equal to 1.772 (see Table V). The calculated ratio E_A^{Mn}/E_A^{Fe} using the simple model of Appendix 2 is found to be equal to 1.955. Such a model is experimentally verified and is supported by the significantly different values of the binding energies (*33*) and of the molar thermodynamic properties (see Introduction: $|\Delta G$ "Mn"$| > |\Delta G$ "Fe"$|$).

2.4. Brittleness and Morphology

The samples of initially pure manganosite at high temperature are variously colored from dark green to brown after quenching, depending on the equilibrium nonstoichiometry (see Table II). The samples obtained by soft quenching (cooling to room temperature under the gas atmosphere used in their preparation) are dark green. The samples obtained under pure hydrogen after slow cooling are pale green and free of Mn_3O_4.

Let us note that the distortion energy is minimized by breaks of crystals (see above). The present discussion allows us to understand why manganosite is more brittle than wüstite, which is comparatively plastic (*35, 36*). It has been observed (*37, 38*) that the cooperative breaks of the bond angles O–*M*–O lead to dislocations (dark color) and cracks on the surface of the grains of manganosite. In addition, the precipitation of Mn_3O_4 in quenched nonstoichmetric samples has been observed by scanning microscopy (acicular crystals) (*37*) in an oxidation layer of manganese, near the manganosite/hausmannite Mn_3O_4 interface (Fig. 9). Nevertheless the disproportionation of $Mn_{1-z}O$ into MnO and Mn_3O_4 seems to be partly avoided in quenched multilayer samples.

Figure 9 shows morphological aspects observed by microscopy on a multilayer sample obtained by oxidation of a manganese sheet. It is seen that the crystalline habit depends on the nonstoichiometry. If defects are present in large concentration, the crystals show an irregular polyhedral aspect. For nearly stoichiometric MnO, pillar or lamellar crystals are observed. In several rare cases Mn_3O_4 has been observed in the grains of manganosite. The morphology of wüstite observed under the same conditions (*38, 39*) is analogous. So it is possible to conclude that

(1) high temperature defects condition the morphology of both oxides,

(2) phenomena during quenching are conditioned by the elastic C_{44} constant and by

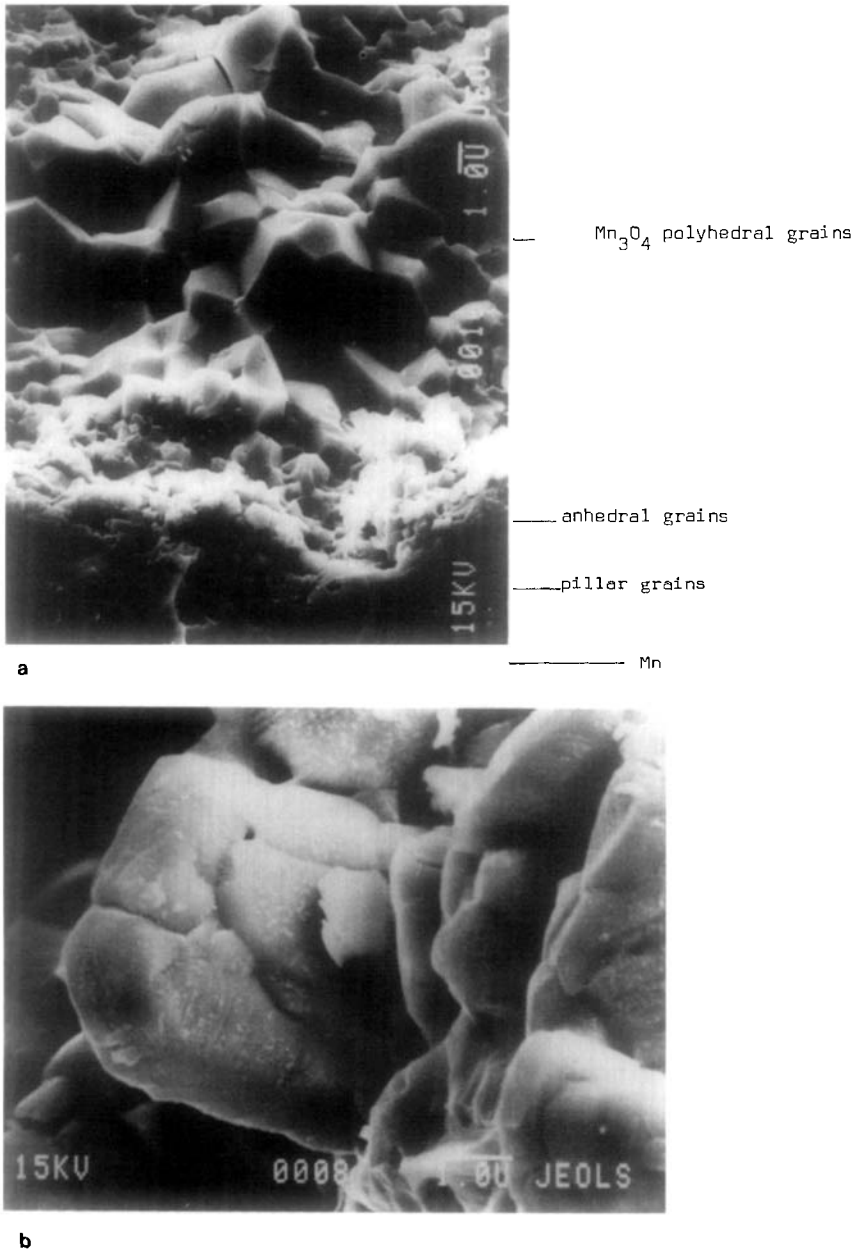

FIG. 9. Morphology of the manganosite layer in an oxidized multilayer sample. (a) Whole layer of manganosite from Mn to Mn_3O_4, (b) manganosite grains with precipitate Mn_3O_4.

clusters, both of which are temperature dependent,

(3) brittleness is conditioned by the C_{44} constant and by clusters in their final form (after quenching),

(4) clusters after or before quenching de-

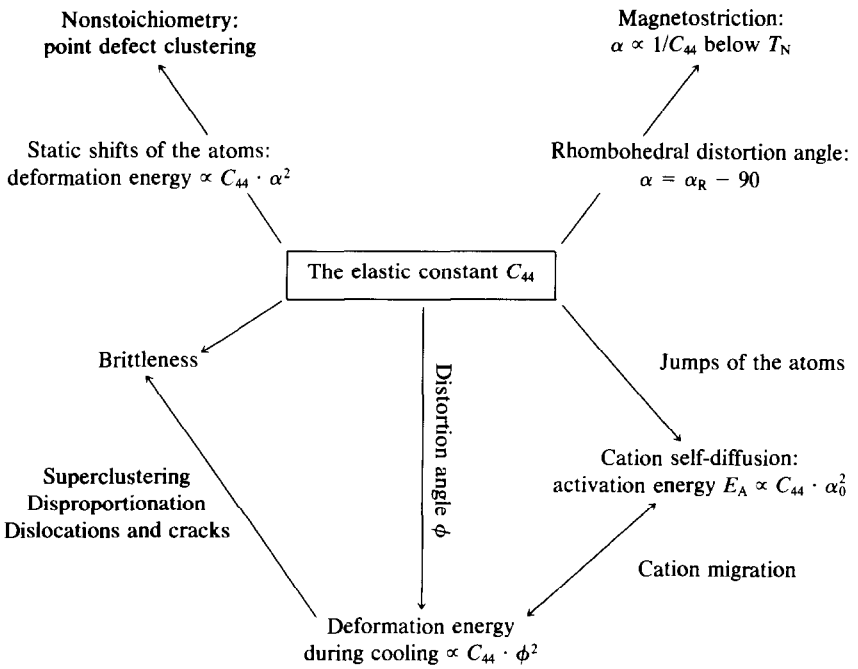

FIG. 10. Summary.

pend on elastic and diffusional properties of the host lattice (however, these properties can be modified by clusters when the latter are sufficiently dilute),

(5) Mn_3O_4 precipates are quite independent of the host lattice in quenched samples from a structural viewpoint (*40*). The problem is quite different at high temperature because the Mn_3O_4 clusters are more dilute.

The role of the C_{44} elastic constant is particularly evident for various properties of the manganese and iron monoxides (see Fig. 10). It is shown how the brittleness and the chemical reactivity can be related to this elastic quantity. This approach should be useful in understanding the complex behavior of industrial materials, principally those found in a blast furnace. It also concerns geophysics. In the near future, the influence of dopant elements such as magnesium and calcium are to be examined (*42*).

Appendix 1

Local and Macroscopic Elastic Properties: Relaxation Effects

Local force constants are directly connected to the macroscopic elastic constants C_{ij}. Angular force constants related to the angles O–*M*–O and *M*–O–*M* in the cubic structures can be connected to local elastic constants or stiffness constants $\tilde{C}_{ij}$. The knowledge of the C_{44} constant leads to the average $\langle \tilde{C}_{44} \rangle_{space}$. In first approximation, one can state that the local angular distortions, assuming a local distortion angle $\tilde{\alpha}$, are related to an energy $\tilde{C}_{44} \cdot \tilde{\alpha}^2$. This is quite true only on the assumption that the elastic constants of the host lattice and of the cluster zones are identical (see discussion in section 2.1).

When the volume of one cluster zone ($\sim L^3$) is increased, the external surface ($\sim L^2$) is increased. However, for a constant

total volume concerning N clusters ($V_T \sim NL^3$) the total surface ($\sim NL^2$) is proportional to V_T/L.

Consequently, when the cluster size is increased, e.g., when the temperature decreases, the total surface energy is decreased, and small clusters are less stable and numerous.

When the C_{44} constant is increased, the total surface energy is increased. That implies a lower stability of the clusters which tends to disappear.

This discussion was initiated in Ref. (*10*). Furthermore it proceeds from the classical theory of the nucleation.

Appendix 2

Relation between the Activation Energy of the Self-Diffusion and the Angular Elastic Constant

The elastic potential in a volume v is a function of the linear distortion ($\Delta a/a$) and the angular distortion α. In the case of a simple monoclinic distortion, the potential energy can be evaluated by the relation

$$E_{el} \sim [\tfrac{1}{2}(C_{11} + C_{12})(\Delta a/a)^2 + \tfrac{1}{2}C_{44}\alpha^2]v.$$

A jump along the [110] direction occurs especially when the angular motions with a large amplitude α are involved, i.e., when the O–*M*–O and *M*–O–*M* angles in the [MO_6] octahedra vibrate in such a way that the shortest *M*–O distances remain unchanged. The elastic potential along the [110] direction can be approximated by the periodic function

$$E_{el}^{[110]} = E_0(1 - \cos 2\alpha).$$

Assuming that the angular vibrational modes are predominant, the linear distortions of the bonds play no significant role.

If a vacant octahedral site is available in the neighborhood of a vibrating atom, its jump into this vacancy corresponds to an angular variation $\alpha = \pi/2$ of the O–*M*–O orbitals; i.e., the O–*M*–O angle is modified from the initial value $\pi/2$ to the maximum value π where E_{el} is maximum. The elastic potential reaches the maximum value $(E_{el})_{Max} = 2E_0 = E_A$ for $\alpha = \pi/2$.

For weak values of α, one obtains the expansion

$$E_{el}^{[110]} \simeq E_A \cdot \alpha^2.$$

Then, the relation available for small distortions with a twofold symmetry axis is

$$E_{el}^{[110]} \simeq \tfrac{1}{2}C_{44} \cdot \alpha^2 \cdot v$$

where $v = N \cdot a^3/8$ is the molar volume. It results that

$$E_A \simeq \tfrac{1}{2}C_{44} \cdot \frac{a^3}{8} \cdot N.$$

For the manganosite and for the wüstite, the values $E_A^{Mn} = 262$ kJ/mole and $E_A^{Fe} = 134$ kJ/mole are obtained respectively. In Table V are given the experimental values $E_A^{Mn} = 218$ kJ/mole and $E_A^{Fe} = 123$ kJ/mole. The agreement is rather good if it is used only as a trend. Therefore, the ratio E_A^{Mn}/E_A^{Fe} is related to the ratio C_{44}^{Mn}/C_{44}^{Fe}, at least in first approximation.

It has recently been shown that this relation applies well to magnesiowüstites. When the magnesium content increases, the C_{44} constant and the activation energy E_A are both increased proportionally (*41*, *42*).

This simplified approach emphasizes the importance of the angular vibrational modes in self-diffusion jumps, but this is of course a roughly simplified description of a much more complicated situation. The complex vibrational modes at work in the self-diffusion are such that E(Mn) > E(Fe), which corresponds to the condition $|\Delta G$ "Mn"$| > |\Delta G$ "Fe"$|$ (see Introduction), but the linear contribution to E_{el} (breaking) does not modify significantly the value of the calculated ratio E_A^{Mn}/E_A^{Fe}.

References

1. W. L. ROTH, *Phys. Rev.* **110,** 1333 (1958).
2. J. B. GOODENOUGH, "Metallic Oxides," Pergamon, Elmsford, N.Y. (1971).
3. P. KOFSTAD, "Nonstoichiometry—Diffusion and Electrical Conductivity in Binary Metal Oxides," Wiley, New York (1972).
4. S. MROWEC, "Defects and Diffusion in Solids, an Introduction," Materials Science Monograph 5, Elsevier, Warsaw (1980).
5. O. TOFT, SØRENSEN, "Nonstoichiometric Oxides," Academic Press, New York (1981).
6. P. VALLET AND C. CAREL, *Mater. Res. Bull.* **14,** 1181 (1979).
7. B. E. F. FENDER AND F. D. RILEY, *J. Phys. Chem. Solids* **50,** 793 (1969). *and in* "The Chemistry of Extended Defects in Non-Metallic Solids," p. 54, North-Holland, Amsterdam (1970).
8. C. CAREL, 1st Round Table Meeting on Fe–Mn–O, Krakow, Poland, Sept. 8–9, 1980, *Bull. Acad. Min. Metall. Krakow,* 8 (1982-R); IXth ISRS, Krakow, Sept. 1–6, 1980, *in* "Materials Science Monographs 10," Vol. 2, p. 596, Elsevier, Warsaw (1982).
9. J. ARABSKI AND C. CAREL, *Bull. Soc. Sci. Bretagne* **55,** 121 (1983).
10. J.-R. GAVARRI AND J. ARABSKI, *Compt. Rend. Acad. Sci. Paris Sér. II* **296,** 949 (1983).
11. J.-F. BERAR, G. CALVARIN, AND D. WEIGEL. *J. Appl. Crystallogr.* **13,** 201 (1980).
12. M. S. JAGADEESH AND M. S. SEEHRA, *Phys. Rev. B* **21,** 2897 (1980) and **23,** 1185 (1981) and *Solid State Commun.* **37,** 369 (1981); with P. SILINSKY, *J. Appl. Phys.* **52,** 2315 (1981); with G. SRINIVASAN, *Phys. Rev. B* **28,** 6542 (1983) and *J. Phys. C.* **17,** 883 (1984).
13. B. TOUZELIN, C. PICARD, P. GERDANIAN, AND M. DODE, "Diagrammes de Phases et Stoechiométrie" (J. P. Suchet Ed.), Vol. 6, p. 51, Masson, Paris (1971).
14. B. MOROSIN, *Phys. Rev. B* **1,** 236 (1970).
15. V. S. MANDEL, V. D. VORONKOV, AND D. E. GROMZIN, *Zh. Eksp. Teor. Fiz.* **63,** 993 (1972).
16. KOHGI, Y., ISHIKAWA, I. HARADA, AND K. MOTIZUKI, *J. Phys. Soc. Japan* **36,** 112 (1974).
17. D. BLOCH, AND R. MAURY, *Phys. Rev. B* **7,** 4883 (1973); with a BARTHOLIN AND R. GEORGES, *Compt. Rend. Acad. Sci. Paris Sér. B* **264,** 360 (1967); with P. CHARBIT, **266,** 430 (1968).
18. S. B. PALMER AND A. WAINTAL, *Solid State Commun.* **34,** 663 (1980).
19. S. S. TODD AND K. B. BONNICKSON, *J. Amer. Chem. Soc.* **73,** 3894 (1950).
20. J. KLEINCLAUSS, R. MAINARD, H. FOUSSE, N. CIRET, D. BOUR, AND A. J. POINTON, *J. Phys. C.* **14,** 1163 (1981).
21. J.-R. GAVARRI, C. CAREL, AND D. WEIGEL, *J. Solid State Chem.* **29,** 81 (1979); **38,** 368 (1981).
22. M. LENGLET, D. LE CALONNEC, J. DÜRR, B. HANNOYER, G. CALAS, J. PETIAU, AND F. JEANNOT, *Mater. Res. Bull.* **18,** 935 (1983).
23. J. B. PRICE, JR., "Chemical and Radiotracer Diffusion in MnO_{1+x}," Ph.D. dissertation, Northwestern University (1968).
24. W. K. CHEN AND N. L. PETERSON, *J. Phys. Colloq.* **34,** Suppl. 11–12, C9-303 (1973); *J. Phys. Chem. Solids* **36,** 1097 (1975) and **43,** 29 (1982).
25. J. JANOWSKI, S. MROWEC, AND A. STOKLOSA, *loc. cit. in* (*8*), 82 (1982-R) and *Bull. Acad. Pol. Sci. Ser. Sci. Chim.* **29** Nos. 1–2, 91 (1981).
26. P. KOFSTAD, *J. Phys. Chem. Solids* **44,** 879 (1983).
27. Y. SUMINO, M. KUMAZAWA, O. NISHIZAWA, AND W. PLUSCHKELL, *J. Phys. Earth* **28,** 475 (1980).
28. J. BERGER, J. BERTHON, A. REVCOLEVSCHI, AND E. JOLLES, *Commun. Amer. Ceram. Soc. C,* 153 (1981); with F. THOMAS, *Solid State Commun.* **48,** 231 (1983).
29. R. JEANLOZ AND R. M. HAZEN, *Nature (London)* **304,** 620 (1983).
30. A. K. CHEETHAM, "Magnetic Ordering in Oxide-Solid Solution, Final Sc. Report for Grant AFOSR-79-0120" (1979/1981); with P. D. BATTLE, *J. Phys. C.* **12,** 337 (1979); with D. A. O. HOPE AND G. J. LONG, *Inorg. Chem.* **21,** 2804 (1982) and *Phys. Rev. B* **27,** 6924 (1983).
31. R. H. CONDIT, "Defects and Transport in Oxides, Battelle Institute Materials Science Colloquia, Sept. 17–22, 1973, Columbus and Salt Fork, Ohio," p. 303, Plenum, New York (1974).
32. B. LEROY, G. BERANGER, AND P. LACOMBE, *J. Phys. Chem. Solids* **33,** 1515 (1972).
33. C. R. A. CATLOW, W. C. MACKRODT, M. J. NORGETT, AND A. M. STONEHAM, *Philos. Mag. A* **40,** 161 (1979).
34. A. N. CORMACK, "Intrinsic Disorder and Defect Structures in Iron Oxides, 2nd Round Table Meeting on Fe–Mn–O, Sept. 14–20, 1983, Krynica, Poland," *Bull. Acad. Min. Metall. Krakow* (1985), in press.
35. G. VAGNARD AND J. MANENC, *Rev. Metall.* **61,** 768 (1964).
36. B. ILSCHNER, B. REPPICH, AND E. RIECKE, *Discuss. Faraday Soc.* **38,** 243 (1964).
37. S. JASIENSKA, J. JANOWSKI, M. GHODI, AND G. NAESSENS, *Rev. ATB Metall.* **23,** 1 (1983); with J. OREWCZYK, *loc. cit. in* (*8*), 61 (1982-R).
38. ST. JASIENSKA, J. JANOWSKI, H. KLIMCZYK, J.

NOWOTNY, J. OREWCZYK, A. SADOWSKI, A. STOKLOSA, AND D. TOMKOWICZ, *loc. cit. in* (*34*).

39. J.-R. GAVARRI, C. CAREL, ST. JASIENSKA, AND J. JANOWSKI, *Rev. Chim. Min.* **18,** 608 (1981).

40. M. S. SEEHRA AND G. SRINIVASAN, *J. Appl. Phys.* **53,** 8345 (1984).

41. W. K. CHEN AND N. L. PETERSON, *J. Phys. Chem. Solids* **41,** 335 (1980).

42. J. R. GAVARRI, C. CAREL, AND J. ARABSKI, "La magnésiowüstite. Evolution structurale et déformation plastique, Xth ISRS, Aug, 27–Sept. 1, 1984, Dijon, France" Elsevier, Amsterdam, in press.